nature communications

Article

https://doi.org/10.1038/s41467-024-50695-1

Strongly coupled edge states in a graphene quantum Hall interferometer

Received: 23 January 2024

Accepted: 18 July 2024

Published online: 02 August 2024

Check for updates

Thomas Werkmeister[1], James R. Ehrets[2], Yuval Ronen[2,3], Marie E. Wesson[1], Danial Najafabadi[4], Zezhu Wei[5,6], Kenji Watanabe[7], Takashi Taniguchi[8], D. E. Feldman[5,6], Bertrand I. Halperin[2], Amir Yacoby[1,2] & Philip Kim[1,2]

Electronic interferometers using the chiral, one-dimensional (1D) edge channels of the quantum Hall effect (QHE) can demonstrate a wealth of fundamental phenomena. The recent observation of phase jumps in a Fabry-Pérot (FP) interferometer revealed anyonic quasiparticle exchange statistics in the fractional QHE. When multiple integer edge channels are involved, FP interferometers have exhibited anomalous Aharonov-Bohm (AB) interference frequency doubling, suggesting putative pairing of electrons into $2e$ quasiparticles. Here, we use a highly tunable graphene-based QHE FP interferometer to observe the connection between interference phase jumps and AB frequency doubling, unveiling how strong repulsive interaction between edge channels leads to the apparent pairing phenomena. By tuning electron density in-situ from filling factor $\nu < 2$ to $\nu > 7$, we tune the interaction strength and observe periodic interference phase jumps leading to AB frequency doubling. Our observations demonstrate that the combination of repulsive interaction between the spin-split $\nu = 2$ edge channels and charge quantization is sufficient to explain the frequency doubling, through a near-perfect charge screening between the localized and extended edge channels. Our results show that interferometers are sensitive probes of microscopic interactions and enable future experiments studying correlated electrons in 1D channels using density-tunable graphene.

Electrons in 1D quantum systems exhibit striking phenomena, including the breakdown of Fermi liquid theory and quasiparticle formation in favor of collective modes[1]. Likewise, electrons confined to two dimensions and subjected to perpendicular magnetic fields exhibit the quantum Hall effects (QHEs)[2]. Although the microscopic details of QHE states are still an active area of research[3,4], their low-energy transport properties are known to be governed by chiral, 1D edge channels[5–8]. These edge channels (ECs) conduct charge ballistically, allowing for phase-coherent electronic experiments[9,10]. In particular, electronic Fabry-Pérot (FP) QHE interferometry[11–13], was performed extensively in GaAs, culminating in the observation of interference phase jumps as evidence for anyonic statistics of fractional quasiparticles[14–17]. Recently, FPs were developed in graphene, which showed Aharonov-Bohm (AB) interference of integer ECs[18–20], with oscillation periodicity set by the magnetic flux quantum for electrons $\Phi_0 \equiv h/e$. Our previous design[18] utilized graphite gates encapsulating the graphene channel, which screened bulk charges. Without such screening layers[21], however, interferometers exhibit 'Coulomb dominated' (CD) behavior

[1]John A. Paulson School of Engineering and Applied Sciences, Harvard University, Cambridge, MA 02138, USA. [2]Department of Physics, Harvard University, Cambridge, MA 02138, USA. [3]Department of Condensed Matter Physics, Weizmann Institute of Science, Rehovot 7610001, Israel. [4]Center for Nanoscale Systems, Harvard University, Cambridge, MA 02138, USA. [5]Department of Physics, Brown University, Providence, RI 02912, USA. [6]Brown Theoretical Physics Center, Brown University, Providence, RI 02912, USA. [7]Research Center for Functional Materials, National Institute for Materials Science, 1-1 Namiki, Tsukuba 305-0044, Japan. [8]International Center for Materials Nanoarchitectonics, National Institute for Materials Science, 1-1 Namiki, Tsukuba 305-0044, Japan. e-mail: pkim@physics.harvard.edu

in which strong coupling of the interfering EC to localized compressible states in the bulk determines the oscillation periodicity and obscures the expected AB oscillations[13,22–24].

When bulk charges were strongly screened, GaAs FPs showed unexpected doubling of the AB oscillation frequency and shot noise corresponding to charge $2e$ when interfering the outermost EC with the bulk of the interferometer in filling $2.5 \le \nu \le 4.5$, suggesting a possibility of 'pairing' of elementary charges[25]. Furthermore, the coherence and periodicity of the interfering outer EC were related to the coherence and the enclosed flux of the adjacent inner EC[26], and the 'pairing' phenomena only occurred when the outer two modes belonged to the same spin-split Landau level[27]. Independently, single-electron capacitance measurements in GaAs quantum dots revealed that tunneling into the edge of the dot corresponded to the entrance of two electrons rather than one for $\nu \ge 2$, and that near $\nu \approx 2.5$ the charging peaks follow doubled magnetic flux frequency[28]. Mechanisms of electron pairing are important questions in emergent phenomena, e.g. high-temperature superconductivity[29] and the even-denominator fractional QHE states in GaAs[30] and bilayer graphene[31,32]. However, theoretical work concerning FP interferometers was able to explain the doubled AB oscillation frequency based on a microscopic model without explicit introduction of electron pairing, though explaining other related phenomena in GaAs remains challenging[33].

In this work, we experimentally address the microscopic mechanism of coupling between QHE edges by elucidating the relation between AB oscillation phase jumps and frequency doubling, employing a highly tunable QHE FP interferometer with strongly screened bulk charge in graphene. We observe periodically modulating interference phase jumps on the outer EC leading to nearly doubled AB oscillation frequency as we increase the electron density in-situ, unveiling a density-induced transition which was not explored in GaAs. We find that strong repulsive interactions between the outermost pair of spin-split ECs can explain both the observation of interference phase jumps and the approximately doubled interference frequency.

Results

Interferometer design and tuning

We designed a graphene-based FP interferometer tuned by a local gate array (Fig. 1a). The FP cavity is defined electrostatically using separated graphite top-gates (Methods and Supplementary Fig. 1), which ensures

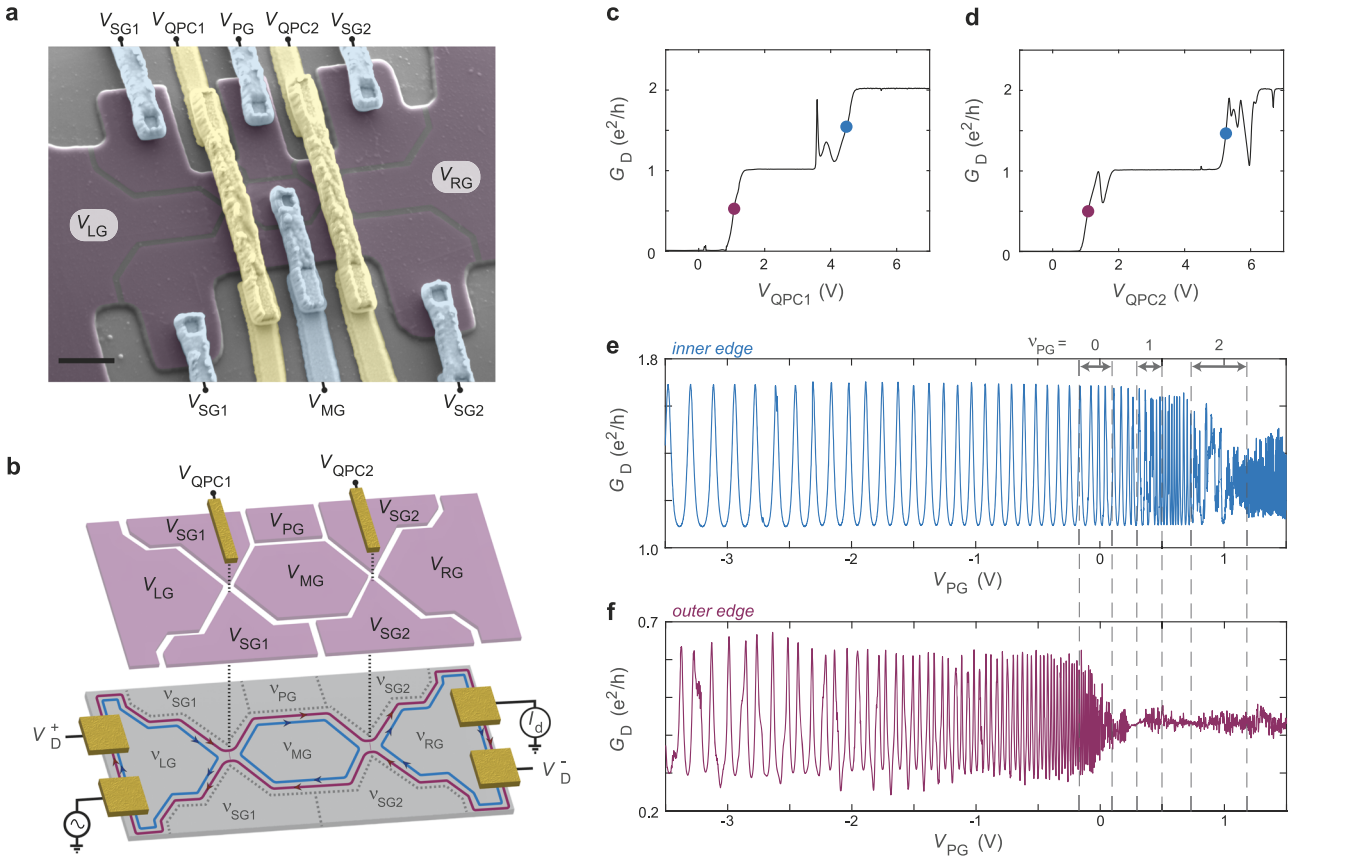

Fig. 1 | Highly tunable Fabry-Pérot interferometer in graphene. a False-color scanning electron microscopy image of a Fabry-Pérot (FP) device identical to the device measured here. The graphite top-gate layer is selectively etched to form 8 separated top-gates (purple). Metal bridges (blue) connect to each graphite top-gate region and two additional bridges (yellow) suspend over the quantum point contacts (QPCs). The lithographic area of the interferometer cavity (area $A = 1.16\mu m^2$) is defined by the central hexagonal top-gate. Scale bar: 1μm. **b** Simplified schematic of the FP tuned so that filling factors $\nu_{LG} = \nu_{MG} = \nu_{RG} = 2$ and $\nu_{SG1} = \nu_{PG} = \nu_{SG2} = 0$ illustrating interference of the partitioned outer edge channel (EC) (red) while the inner EC (blue) forms a closed annulus inside the FP. Voltage V_i applied to the top-gate labeled 'i' tunes the local filling factor ν_i. Voltages V_{QPC1} and V_{QPC2} applied to the suspended metal bridges selectively gate the QPC constrictions through the etched graphite gaps, tuning the QPC transmissions. We measure the diagonal conductance $G_D = I_d/(V_D^+ - V_D^-)$, where $V_D^\pm$ and I_d are measured voltages in (±) probes and drained current, respectively. See Supplementary Fig. 1 for the full device details. In addition to magnetic field, we tune the interference phase using voltage V_{MG} on the 'middle gate' or V_{PG} on the 'plunger gate'. **c** Conductance as a function of V_{QPC1} with $V_{QPC2} = 7$V (i.e. $T_{QPC2} = 2$) demonstrating QPC1 tunings to interfere outer EC (red dot) and inner EC (blue dot) in $\nu = 2$. See Supplementary Fig. 3 for QPC tuning details and voltages set on the other gates to form the necessary QPC saddle-points to acquire this data. **d** Same type of plot as (**c**), but demonstrating QPC2 operation instead of QPC1. **e**, **f** Characteristic FP oscillations as a function of V_{PG} for the inner EC and outer EC, respectively, at the QPC tunings indicated in (**c**) and (**d**). Vertical dashed lines indicate edges of plateaus of filling factor ν_{PG}. All data is at fixed magnetic field $B = 6$T.

a high channel quality and allows a high degree of density tunability in-situ. Metal bridges contact each top-gate, and we additionally suspend metal bridges over the two quantum point contacts (QPCs), illustrated in Fig. 1b. By applying voltages V_{QPC1} and V_{QPC2} to these suspended bridge gates, we can tune the transmission of each QPC independently while keeping the filling factor of the surrounding regions fixed (Supplementary Note 1).

In our experiments, we measure the diagonal conductance G_D, as defined in Fig. 1b and Supplementary Fig. 1. In the regime that we study, $G_D = \frac{e^2}{h}\nu_{QPC}$ where ν_{QPC} counts the number of edge channels transmitted through the device, with a partially transmitted channel counted as fraction[34,35]. To characterize the QPC transmissions, we measure G_D as a function of the bottom-gate voltage and split-gate voltage for each QPC with the bulk of the interferometer tuned to $\nu = 2$ at $B = 6$T (Supplementary Fig. 3). At $\nu = 2$, there are two spin-split Landau levels, of which the lower energy spin species hosts an EC closer to the effective boundary of the sample. Hence, we refer to the EC belonging to the lower (higher) energy spin species as the 'outer' ('inner') EC. Once appropriate bottom-gate and split-gate voltages are set, we tune V_{QPC1} and V_{QPC2}, voltages applied on the suspended bridges to control the individual QPC transmissions. Figure 1c, d shows the measured G_D as a function of V_{QPC1} and V_{QPC2}, respectively, with the other QPC fully open (i.e. $\nu_{QPC2} = 2$ and $\nu_{QPC1} = 2$, respectively). G_D exhibits plateaus at $(0,1,2)\frac{e^2}{h}$, corresponding to (neither, outer, both) ECs transmitted. In this regime, we define $T_{QPC} \equiv G_D \frac{h}{e^2}$ as the transmission of the QPC[34], where $0 < T_{QPC} < 1$ corresponds to a partially transmitted outer EC and $1 < T_{QPC} < 2$ corresponds to a partially transmitted inner EC.

Tuning to partial transmission of the inner EC for both QPCs, $T_{QPC1} = T_{QPC2} = 1.5$, we observe high-visibility conductance oscillations as a function of plunger gate voltage V_{PG}, which tunes the filling factor ν_{PG} under the plunger gate, in Fig. 1e. Similarly, we tune to $T_{QPC1} = T_{QPC2} = 0.5$ and measure conductance oscillations on the outer EC in Fig. 1f. In both cases, oscillations are largest for $\nu_{PG} < 0$, which corresponds to a fully gate-defined interference path since electrons are depleted under the plunger gate. Increasing ν_{PG} brings the interfering edge closer to the etched graphene boundary, inducing dephasing[18]. Notably, the inner EC oscillations survive until $\nu_{PG} = 2$, when it flows close to the etched boundary of the graphene, while the outer EC reaches the boundary by $\nu_{PG} = 1$. Another difference is the apparent irregularity of the oscillations on the outer EC compared to the inner EC, which we will understand in this work.

Phase jumps and AB oscillation frequency transition

High-visibility oscillations allow us to probe the dependence of interference phase θ on magnetic field variation δB and gate voltage variations, which distinguishes the AB from the CD regimes[13,15,18,19,22]. For small variations in field and gate voltages in the AB regime, we expect $\delta\theta/2\pi \approx A\delta B/\Phi_0 + C_{PG}\delta V_{PG}/e + C_{MG}\delta V_{MG}/e$, where A, C_{PG}, and C_{MG}, are the (approximately constant) area enclosed by the interfering EC, interfering EC−plunger gate capacitance, and interfering EC − middle gate capacitance, respectively. Importantly, V_{MG} also directly tunes the electron density in the interferometer, so sweeping V_{MG} over a large range will change the FP cavity filling factor ν_{MG}. To calibrate the filling that we expect in the cavity, we first measure standard Hall conductance in the region gated by V_{LG} (see Supplementary Fig. 1e) and observe conductance plateaus (Fig. 2a). Since the top gates are identically coupled to the channel directly beneath them, an identical sweep of V_{MG} will tune ν_{MG} through the same filling factors. Data in the remaining panels of Fig. 2 were taken with the QPCs set to $T_{QPC1} = T_{QPC2} = 0.5$ i.e. partially transmitting the outer EC. Near the lowest density of the $\nu_{MG} = 2$ plateau (Fig. 2b), we observe a typical AB interference pattern. Constant phase stripes ($\delta\theta = 0$) trace out a negative slope $\delta V_{PG}/\delta B$ with magnetic field period ΔB yielding $\Phi_0/\Delta B = 1.13\mu\text{m}^2$, matching the designed area $A = 1.16\mu\text{m}^2$. Plunger gate period ΔV_{PG} yields $1/\Delta V_{PG} = 19.2\text{V}^{-1}$. Increasing ν_{MG} using V_{MG} reveals more complicated interference patterns in Fig. 2c, d. Periodic shifts in the interference pattern persist and modulate until near the center of $\nu_{MG} = 4$, as seen in Fig. 2e, when a simple stripe pattern returns. However, now $\Phi_0/\Delta B = 2.32\mu\text{m}^2$ and $1/\Delta V_{PG} = 36.3\text{V}^{-1}$, both approximately doubled from Fig. 2b. Since A is fixed, a doubling of $\Phi_0/\Delta B$ indicates oscillations with $\Phi_0/2 = h/2e$ periodicity instead of Φ_0 so that $\Phi_0/2\Delta B = 1.16\mu\text{m}^2$. Similarly, assuming a fixed C_{PG}, then $1/\Delta V_{PG}$ doubling corresponds to adding twice as many electrons to the system per flux quanta. Both could be interpreted as an effective charge $e^* = 2e$ for the interfering particle, as argued in GaAs[25–27], but our observations indicate a different interpretation in our graphene-based interferometer.

Importantly, we can observe the entire density-tuned transition to the AB frequency-doubled regime at fixed B by sweeping V_{MG} and observing oscillations with V_{PG}, as shown in Fig. 2f. Remarkably, the frequency transition occurs continuously. From the top panel, Φ_0 interference is apparent. As V_{MG} increases, periodic phase jumps begin to appear. Both the V_{MG} spacing and magnitude of the phase jumps increase, until eventually the most apparent periodicity corresponds to $\Phi_0/2$ oscillations (i.e., doubled frequency $2\Phi_0^{-1}$).

To better understand the phase jumps, we use a general relation between charge and phase in FP interferometers[36]. When a single EC passes through the two constrictions with weak backscattering, the interference phase seen by the device at zero temperature is $\theta = 2\pi Q + \theta_0$, mod 2π, where Q is the total electron charge (in units e) in the region between the two scattering points and θ_0 is a constant for small variations in B, V_{PG}, and V_{MG}. In our experimental regime, $\nu \geq 2$, we expect this relation to hold with $Q = Q_1 + Q_2$, where Q_1 is the total charge residing in the lowest spin-split Landau level and Q_2 is the charge in the higher energy spin state (and also higher Landau levels). Q_1 can vary continuously since the outer EC is connected to the source and drain charge reservoirs. In contrast, Q_2 is required to be integer, as the corresponding energy levels are isolated through the incompressible QHE bulk. An integral change in Q_2 has no observable effect on the interference signal unless it produces a non-integral change in Q_1 due to Coulomb coupling between the two types of charge. Hence, we can redefine θ to include only the charge Q_1 in the lowest spin-split Landau level, and the values Q_1 in the ground state of the interferometer determine θ. Following similar models used to understand the CD regime[15,24,37] and considering small changes in Q_1 and Q_2, we expand the change in ground state energy $E = K_1\delta Q_1^2 + K_2\delta Q_2^2 + 2K_{12}\delta Q_1\delta Q_2$, where K_i is the charging energy of the charge species i and K_{12} describes the mutual capacitive coupling between them. Energetic stability requires that $|K_{12}|^2 \leq K_1K_2$. Within this capacitive coupling model, when Q_2 increases by 1, the charge Q_1 correspondingly decreases by a discrete (generically non-integral) amount ΔQ_1 to screen the added charge, leading to a phase shift $\Delta\theta/2\pi = \Delta Q_1 = -K_{12}/K_1$.

By taking 1D fast Fourier transforms (FFTs) along lines parallel to the phase jumps[14,15], we extract several values of $\Delta\theta/2\pi$ near the center of the periodicity transition in Fig. 3a. We observe that the locations where the phase jumps occur (marked in Fig. 3b) follow a steeper slope than the slope $\delta V_{PG}/\delta V_{MG}$ of constant phase lines of the main interference oscillation in the V_{MG}-V_{PG} planes. A steeper slope also occurs in the B-V_{PG} plane (Fig. 2c, d). Moreover, these phase jump lines have negative slopes $\delta V_{PG}/\delta B < 0$, like the constant phase lines of AB oscillations. This observation is in sharp contrast to the phase jumps reported in the FP interferometer operated in the fractional QHE regime[14,15] or in the FP interferometer operated in the integer CD regime[37], where phase jump lines follow positive slope $\delta V_{PG}/\delta B > 0$. The different slope suggests a different structure to the energy levels that are being populated in our sample. Considering that the outer EC is partitioned at the QPCs, while the inner ECs are well isolated, we hypothesize that the charging events seen as phase jumps represent

https://doi.org/10.1038/s41467-024-50695-1

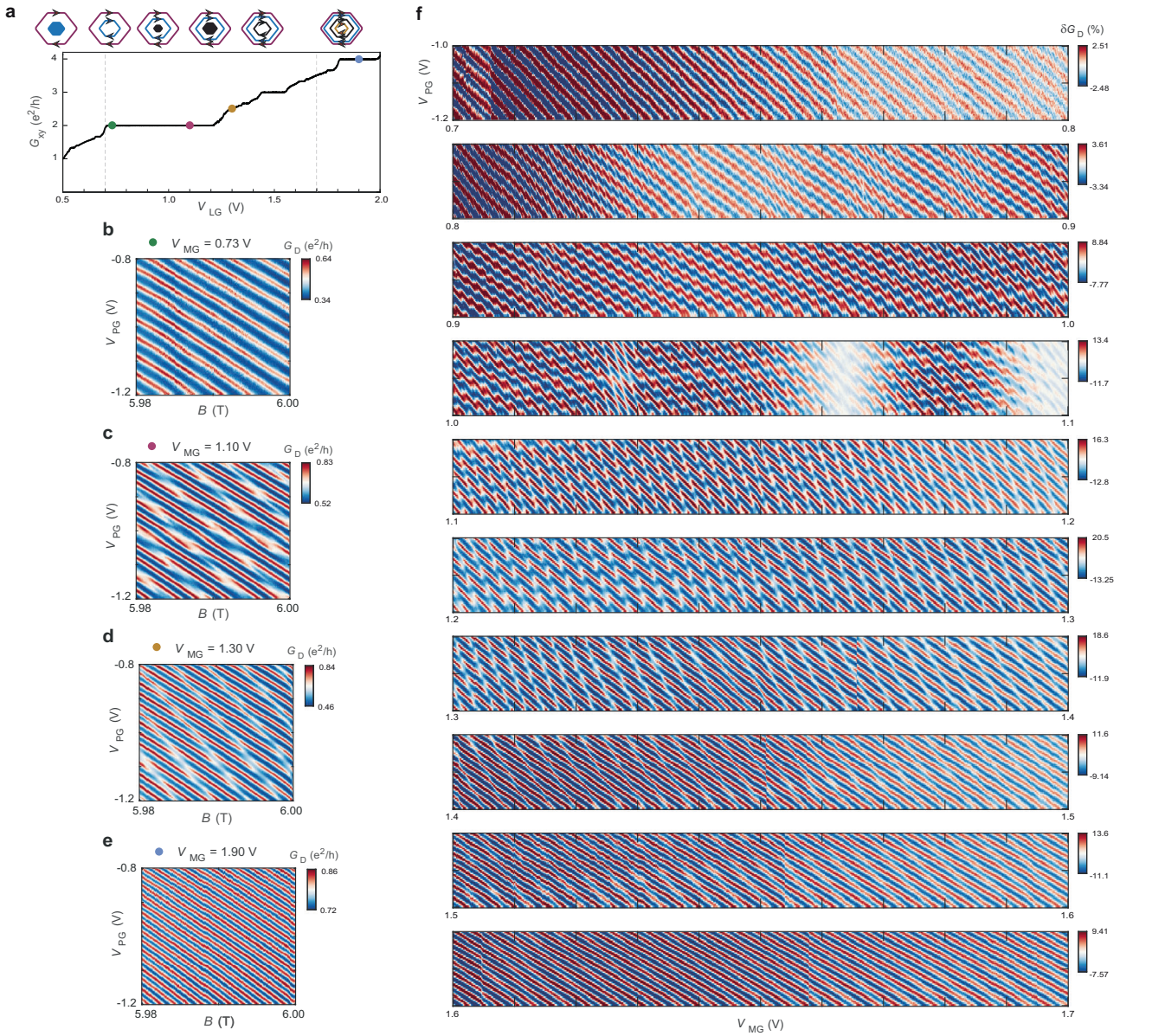

Fig. 2 | Density-tuned Aharonov-Bohm frequency doubling transition of outer EC. a Hall conductance G_{xy} in the region gated by V_{LG}, demonstrating that V_{LG} (equivalently, any of the top gates) tunes the filling ν underneath it at a fixed magnetic field $B = 6$T. Colored dots indicate the filling (set by equivalent V_{MG} voltages) at which interference data are shown in (**b**–**e**); vertical dashed lines show the range of V_{MG} swept for (**f**). Top inset: schematic of compressible regions expected in the FP cavity when V_{MG} is swept. **b**–**e** Conductance G_D oscillations on the outer EC with V_{PG} and B, for each of the indicated V_{MG} values. **f** G_D oscillations on the outer EC with V_{PG} and V_{MG}, for V_{MG} swept continuously over the transition from apparent h/e to $h/2e$ oscillations periodicity, at $B = 6$T. G_D is plotted as a percentage of $\frac{e^2}{h}$ deviation from the average value calculated for each fixed V_{MG} linecut and subtracted off. Further phase jumps or periodicity changes are not observed past $V_{MG} \approx 1.7$V (checked up to $\nu = 7$). QPCs are retuned to maintain transmissions $T_{QPC1} = T_{QPC2} = 0.5$ over the dataset while $\nu_{LG} = \nu_{RG} = 2$ and $\nu_{SG1} = \nu_{SG2} = 0$ are fixed.

charge added to the annular, closed inner EC, illustrated in Fig. 3. The dominant coupling K_{12} is directly between the outer and inner $\nu = 2$ ECs. Any charges added to higher Landau levels or to localized states in the bulk are not measurably coupled to the outer EC, presumably because of effective screening by the gates.

AB frequency doubling from strongly coupled QHE edge states

We provide further evidence for capacitively coupled QHE edges tuning the AB frequency in Fig. 4. At fixed V_{MG} in the transition regime, we compare interference in the B-V_{PG} plane for the inner EC, Fig. 4a, to the outer EC, Fig. 4c. This direct comparison is only possible because we can control QPC transmissions independently of bulk filling. We observe that the slope of the oscillation maxima on the inner EC (dotted lines in Fig. 4a) matches the slope of the phase jump lines on the outer EC (dotted lines in Fig. 4c). Reducing the transmission for the inner EC, the interference maxima in Fig. 4a become sharper charging resonances, corresponding to charge $Q_2 \to Q_2 + 1$ through the inner EC. When the transmission of the inner EC vanishes, the inner EC is fully disconnected from the source and drain charge reservoirs, and the outer EC is now partitioned at the QPCs to form a new interference path (shown in the left inset in Fig. 4c). Since the bulk density and electrostatic configurations for Fig. 4a and Fig. 4c are identical, the regions in between the phase jump lines in Fig. 4c correspond to fixed Q_2, and we see that the interference phase on the outer EC shifts when the charge on the inner EC discretely changes.

Taking Fourier transform of the interference signal provides further understanding of interactions between the two ECs involved in

https://doi.org/10.1038/s41467-024-50695-1

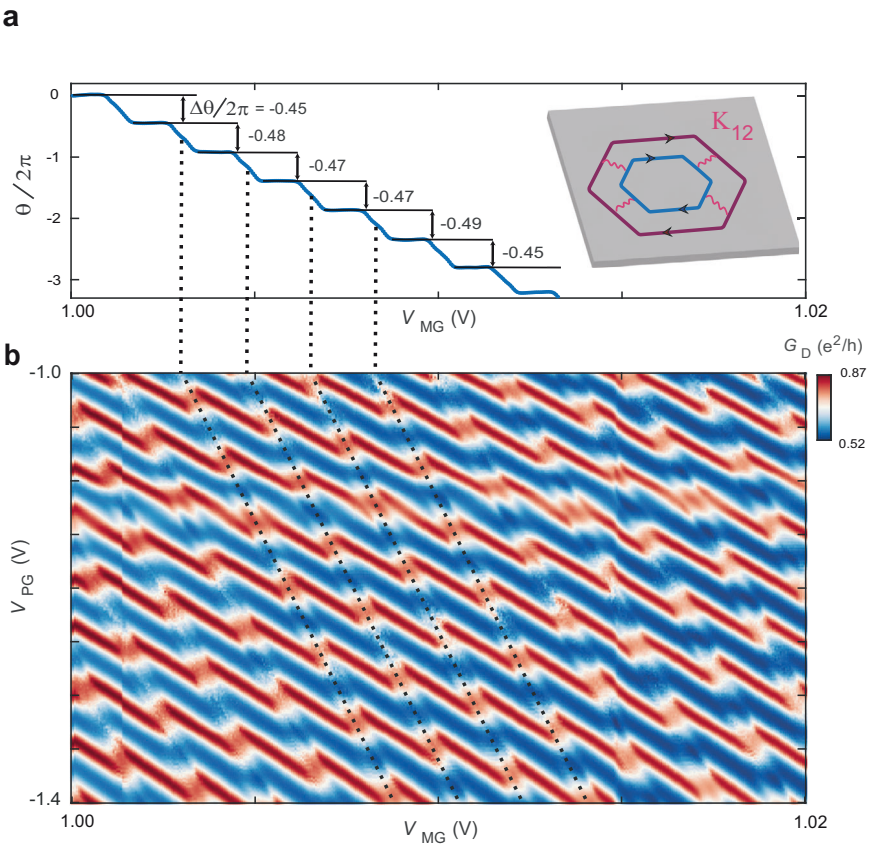

Fig. 3 | Phase jump extraction in the transition regime. a Phase θ of the 1D FFT extracted along linecuts parallel to the phase jumps in (**b**). The phase is evaluated at the dominant frequency in the FFT amplitude spectrum for the linecuts in between phase jumps. A linear increase in phase extracted from regions without phase jumps is subtracted off to make the phase jump magnitude evident as the vertical shift between plateaus in panel (**a**). From this data we extract an average $\Delta\theta/2\pi \approx -0.47$, reflecting approximately half of an electron repelled from the outer EC for each charge added to the inner EC within this range of V_{MG}. Inset: illustration of the coupling K_{12} between the outer and inner ECs contributing to the phase jumps. **b** Conductance G_D oscillations on the outer EC with V_{PG} and V_{MG} near the center of the transition regime showing periodic phase jumps along the dashed black lines. Note that increasing V_{MG} adds electrons to the system or equivalently increases phase, so the phase jumps correspond to negative shifts in phase i.e., repulsion of electrons from the FP cavity. Similar interference patterns are observed in both the strong and weak QPC backscattering regimes (Supplementary Fig. 4) as well as at elevated temperatures (Supplementary Fig. 5).

the interference. Figure 4b, d shows the 2D FFT of the conductance oscillations in Fig. 4a, c. For interference of the inner EC (Fig. 4b), we observe a simple FFT pattern of peaks corresponding to the fundamental frequency of the inner EC $\boldsymbol{f}_i$, a vector containing the peak position in the 2D FFT, and its harmonics ($n\boldsymbol{f}_i$, where n is an integer). The FFT pattern of the outer EC interference (Fig. 4d) exhibits a more complicated lattice of Fourier peaks. If we label one of the dominant peaks as the fundamental frequency of the outer EC, $\boldsymbol{f}_o$, we can then identify the rest of the peaks by addition or subtraction of the same vector $\boldsymbol{f}_i$ evident in the inner EC data. The lowest order peaks correspond to the sum $\boldsymbol{f}_{o+i} = \boldsymbol{f}_o + \boldsymbol{f}_i$ and the difference $\boldsymbol{f}_{o-i} = \boldsymbol{f}_o - \boldsymbol{f}_i$. We show a similar Fourier lattice construction in Supplementary Fig. 6 for interference in the B-V_{MG} plane.

By tuning V_{MG}, we modulate the filling factor of the interferometer cavity in a wide range and observe the evolution of the interference patterns and corresponding peaks for the outer (inner) EC in Supplementary Fig. 7 (8). As in Fig. 2, phase jumps appear only within the periodicity transition. Figure 4e shows the average magnitude of individual phase jumps as a function of V_{MG}. We find that the phase jump continuously evolves from $\Delta\theta/2\pi \approx 0$ ($V_{MG} < 0.6$V) through the periodicity transition to $\Delta\theta/2\pi \approx -1$($V_{MG} > 1.6$V), corresponding to the strongly coupled limit $K_{12}/K_1 \approx 1$. The transition regime marked by non-trivial phase jumps spans from the appearance of the inner EC ($V_{MG} \approx 0.6$V) to the strongly coupled outer two EC limit ($V_{MG} \approx 1.6$V).

The Fourier peaks' evolution tuned by V_{MG} provides further insight into the interaction between ECs. Figure 4f displays the normalized Fourier peak intensity as a function of V_{MG}.The amplitude of the Fourier peak $\boldsymbol{f}_o$ decays through the transition regime ($0.6\text{V} < V_{MG} < 1.6\text{V}$), replaced by $\boldsymbol{f}_{o+i}$ as the dominant peak. We plot the magnetic field frequency multiplied by Φ_0 (Fig. 4g) and the plunger gate frequency (Fig. 4h), respectively, for each of the lowest-order peaks $\boldsymbol{f}_o$,$\boldsymbol{f}_i$,$\boldsymbol{f}_{o+i}$, and $\boldsymbol{f}_{o-i}$ as a function of V_{MG}. At the beginning of the transition regime where the ECs are not interacting, both $\boldsymbol{f}_o$ and $\boldsymbol{f}_{o+i}$ approach the corresponding AB frequency $\Phi_0^{-1} = e/h$ through the designed area. As V_{MG} increases, however, $\boldsymbol{f}_o$ stays nearly unchanged, while $\boldsymbol{f}_{o+i}$ increases to reach the doubled value $2\Phi_0^{-1}$. The experimental observation that the dominant peak in the frequency-doubled regime corresponds to $\boldsymbol{f}_{o+i}$ precludes the possibility of $2e$ charge pairing within the outer EC alone.

Instead, our frequency-doubled regime arises from Coulomb interaction between the spin-split ECs combined with charge quantization on the inner EC (Methods). Electrons would naturally tend to enter the inner EC at frequency $\boldsymbol{f}_i$, but, due to charge quantization, cannot enter continuously. Hence, as the magnetic flux increases continuously, the area enclosed by the inner EC must shrink to maintain fixed charge. During this shrinking process, electron charge is transferred continuously into the interior, leaving missing electron charge between the outer and inner ECs. In the strongly coupled EC limit, this missing charge attracts an equal charge onto the outer EC for

https://doi.org/10.1038/s41467-024-50695-1

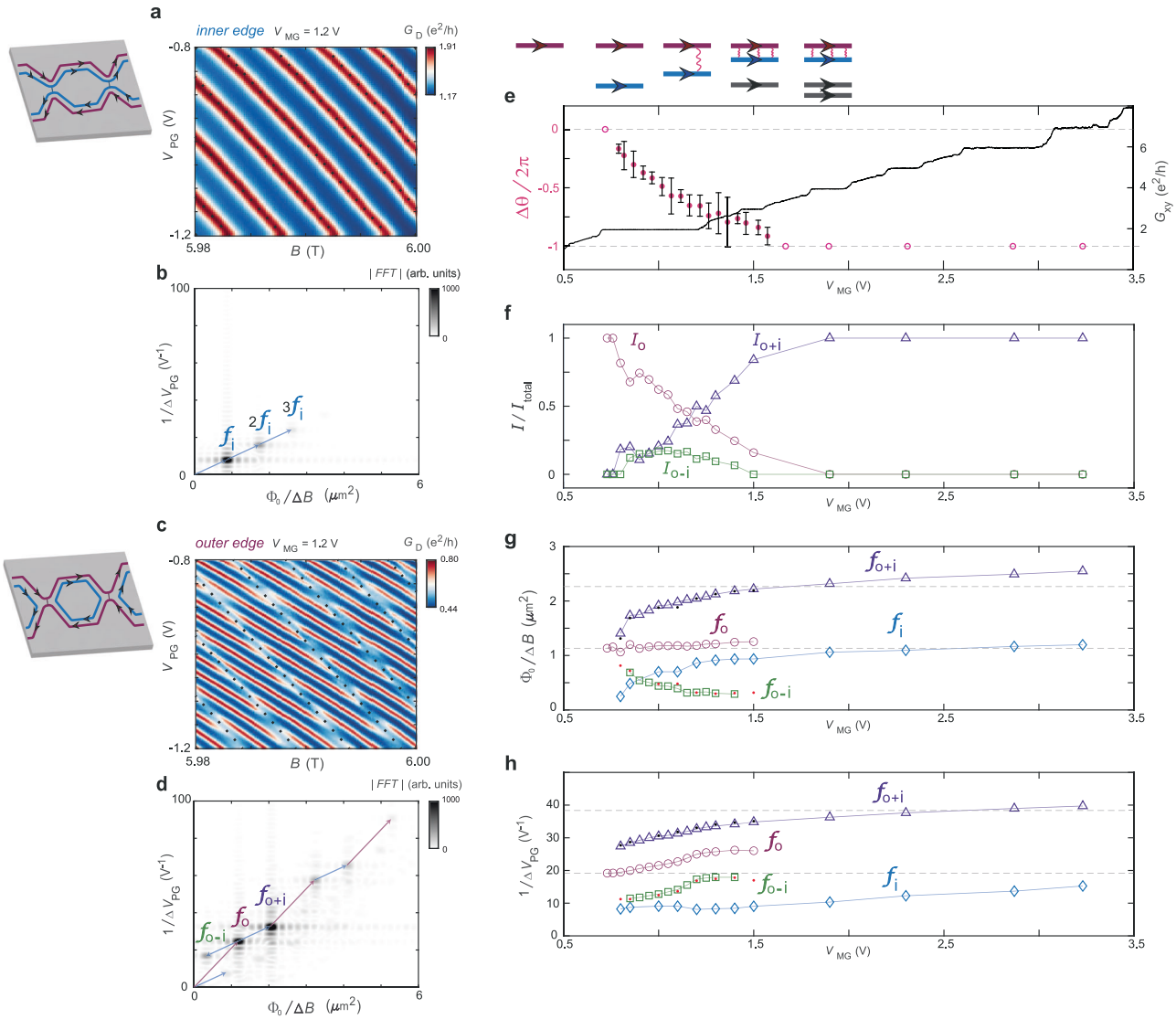

Fig. 4 | Comparison of inner and outer EC interference and couplings across transition. a Conductance G_D oscillations on the inner EC ($T_{QPC1} = T_{QPC2} = 1.5$) with V_{PG} and B, for $V_{MG} = 1.2$V. Dotted black lines highlight conductance maxima. Left inset: illustration of inner EC interference configuration. **b** 2D FFT of the G_D oscillations in (**a**) showing peak f_i (vector corresponding to blue arrows) and its harmonics, where $\Phi_0 \equiv h/e$. **c** G_D oscillations on the outer EC ($T_{QPC1} = T_{QPC2} = 0.5$) at the same density set by V_{MG}. Dotted black lines with identical slope to (**a**) highlight phase jumps. Left inset: illustration of outer EC interference configuration. **d** 2D FFT of oscillations in (**c**) showing the peaks f_o (red arrows), f_{o+i}, and f_{o-i} and their harmonics. **e** Magnitude of the phase jump on the outer EC as a function of V_{MG}. Each data point is averaged over a ~0.25V range in V_{MG}; error bars indicate ±1 standard deviation in this range. Unfilled data points represent zero observable phase jumps over the range, hence we infer a magnitude of 0 or −1. G_{xy} of the device taken in an identical measurement to Fig. 2a, reflecting the expected filling ν_{MG}, is plotted for reference. Top inset: cartoon of the outer and inner EC evolution with increasing V_{MG}. **f** Magnitudes I_o, I_{o+i}, and I_{o-i} of the respective peaks f_o, f_{o+i}, and f_{o-i} as a function of V_{MG}. I_o, I_{o+i}, and I_{o-i} are normalized by the sum $I_o + I_{o+i} + I_{o-i}$ to show their relative contributions. Each data point is extracted from a 2D FFT (Supplementary Fig. 7). **g** Magnetic field frequency multiplied by Φ_0 for peaks f_o, f_i, f_{o+i}, and f_{o-i} tracked through the transition. Note that f_i is measured from a separate measurement of interference on the inner EC (Supplementary Fig. 8). **h** Same as (**g**) but for plunger gate frequency. Horizontal dashed lines in (**g**, **h**) indicate the corresponding f_o and $2f_o$ values before the transition. Black (red) dots show calculated $f_o \pm f_i$ from outer and inner EC data, which match the peaks identified as f_{o+i} and f_{o-i}, respectively.

screening. In the absence of this screening effect, charge is continuously added to the outer EC with frequency f_o according to the increased AB phase. In the coupled ECs, the combination of the screening-induced charge and the natural AB effect results in the outer EC charging at a frequency f_{o+i}. Therefore, the interference phase follows f_{o+i}. In addition to this continuous charging effect, electrons can tunnel into the inner EC from the external reservoirs. As previously discussed, each electron addition repels some electron charge from the outer EC, causing the negative interference phase shifts that we observed. For larger values of V_{MG}, as the bulk density increases, the inner and outer EC move closer together, and the system approaches the strong coupling limit, where the phase jumps are close to -2π and unobservable, reflecting a full electron charge screening. Moreover, as the inner and outer ECs asymptotically enclose the same area, set by the confining potential of the device, the frequency f_{o+i} approaches $2\Phi_0^{-1}$.

Note: a concurrent work also observed apparent AB frequency tripling, corresponding to the sum of the three $\nu = 3$ edge channel frequencies[38]. The framework that we developed here can be expected to naturally explain this observation, since in devices utilizing the graphene crystal edge, the sharp confining potential can lead to multiple ECs developing within a few magnetic lengths of the edge[8].

The combination of reduced spatial separation and reduced screening by nearby graphite gates may account for the observation of apparent tripling, arising from the outer EC screening both internal localized ECs.

Discussion

We have investigated phase jumps and AB frequency modulation in a highly tunable graphene QHE FP interferometer with coupled co-propagating edge modes. We identify that interference phase jumps are related to the single electron charging events in the inner EC, and the transition of the AB frequency can be connected to the corresponding screening effect of the outer EC. As V_{MG} increases, the EC coupling becomes strong and the AB frequency doubles, indicating a near-perfect screening between the ECs. Thus, our experimental observation supports the proposal that AB frequency doubling can be explained without explicitly introducing electron pairing within the outer two ECs[33]. In other words, a half flux quantum introduced in the two strongly coupled ECs can bring a full charge from the external reservoir and a 2π evolution of the observed interferometer phase.

Our observations do not exclude the possibility of further correlation effects in the strongly coupled ECs; instead, the tunably coupled ECs discovered here provide a system to test the emergence of electron correlations in 1D systems[39]. However, AB frequency multiplication, which we explained within a single particle picture, cannot substantiate the correlation effect. Further experiments probing the transition from the weakly to strongly coupled limit, such as shot noise[25,40,41], finite-bias dependence[15,42], energy relaxation[43], and high-frequency transport[44–46] will provide further insight into the ground state and excitations. More generally, inter-edge screening could affect interferometry in fractional fillings containing multiple ECs[42,47–49], though fractional QHE experiments so far appear to be in the weak coupling regime[42,50]. The recent observations of interference in fractional quantum Hall states using similar bilayer and monolayer graphene devices[51–53] will enable further experiments to probe the interacting co-propagating fractional QHE edge modes, where it remains unclear whether the strong coupling regime can be realized between fractional edge channels.

Methods

Sample preparation

The monolayer graphene stacks with hBN and graphite encapsulation used in this study were fabricated using the standard polycarbonate (PC) polymer dry transfer method (ref. 18). The graphite top-gates and bottom-gate, which encapsulate the graphene channel after stacking, are crucial to screen charge disorder from the graphene channel, stabilizing robust integer and fractional QHE states at low magnetic fields (Supplementary Fig. 2). The stack used for all data shown here had a top (bottom) hBN thickness of 49 (27) nm. After adhering the stack to a substrate and annealing in vacuum at 300 °C, the top gate was first etched into a simplified shape by reactive ion etching in an inductively coupled plasma etching chamber with 30 W O_2 plasma using a polymethyl methacrylate (PMMA) resist patterned with electron-beam lithography as the etch mask. Next, a full etch through the entire stack was performed to define all outer boundaries. This etching was in several steps: first a pure 30 W O_2 etch remnants of the top graphite; then a 30 W process O_2/CHF_3 to etch through the underlying hBN, graphene, and hBN; and finally another 30 W O_2 etch to remove the bottom graphite. Next, edge contacts to the exposed graphene were made by a 30 W CHF_3 etch on the exposed hBN/graphene/hBN contact regions and thermal evaporating 2/7/150 nm of Cr/Pd/Au at an angle with rotation. Then, air bridge contacts were made to the top-graphite in various locations using a bilayer PMMA process followed by a short 20–25 s 30 W O_2 plasma PMMA residue clean and thermal evaporation of 2/7/350 nm Cr/Pd/Au. Then, to etch the ~100 nm width trenches to separate the top graphite regions, a thinner PMMA resist was used and again a reactive ion etch with gentle 30 W O_2 plasma alone was done in ~1 minute steps. In between etches, the two-probe resistance between each bridge-contacted gate was checked until they were all separated. Finally, bridge contacts to the separated central hexagon gate and suspended bridges over the QPC regions were deposited. See Supplementary Fig. 1 for more details on the fabrication process and the final device.

Measurements

The 8 top graphite gates in the device were separately controlled to set filling factors in each region at perpendicular magnetic field B, since Landau level filling factor (also simply called 'filling') $\nu \equiv n_e/n_\phi$, where $n_\phi = eB/h$ and n_e is the areal electron density. At the region in the middle of the top-gate split-gates, where the graphite is etched away for a separation of ~150 nm, the electrostatics are tuned to create a saddle-point potential at the QPC. See Supplementary Note 1 for details of this tuning process. Once an approximate saddle-point is formed at the QPCs using the graphite top-gates and bottom-gate, the suspended metal bridges over the QPCs are tuned to precisely set transmissions T_{QPC1} and T_{QPC2}. The neighboring top-gates screen out stray fields generated by the suspended bridges such that V_{QPC1} and V_{QPC2} are primarily coupled to the graphene at the saddle-point of the QPCs. We interpret non-integer values $0<T_{QPC}<1$ as a transmission probability for electrons in the outer EC, which is partially transmitted, while for $1<T_{QPC}<2$, $T_{QPC}-1$ gives the transmission probability for the inner EC.

Experiments were performed in an Oxford wet dilution system with base temperature ~20 mK and estimated ~20–25 mK electron temperature. The 24 DC measurement lines of the fridge were carefully thermalized through Thermocoax cables and 3 Sapphire plates between room temperature and the mixing chamber. A series of lumped element Pi and RC filters at the mixing chamber reduced electronic noise and ensured low electron temperature. Unless otherwise noted, a constant 6 T perpendicular magnetic field was applied. Measurements were taken using standard low-frequency lock-in amplifier techniques with a typical AC excitation current of 1 nA at 17.77 Hz applied to the sample and simultaneously measured AC voltage drops and drained current. Graphite and suspended bridge gates were controlled with a house-made, low-noise 16-bit D/A voltage source. Bias dependence (see Supplementary Note 4) was taken by voltage biasing instead and adding in a DC bias at the source. Simultaneously, the DC voltage drop V_D was measured on the same probes measuring the AC conductance so that the accurate voltage drop across the FP cavity was known. All data collected and analysis programs have been made available.

Estimation of the coupling strength

Although we have not attempted a detailed calculation of the coupling constants important for our analysis, we can at least advance some qualitative arguments for the trend that emerges from our analysis. The edge of the sample consists of alternating compressible and incompressible stripes whose width is set by electrostatics[6]. ECs are located in compressible stripes. It may be expected that the outermost EC is located along an electron density contour where the local Landau-level filling factor is ~ 0.5, while the second EC is located along a contour with filling ~1.5. Due to residual disorder and electron-electron interactions, the Hall plateau at $\nu = 2$ will set in when the bulk filling is smaller than 2, though larger than 1.5. The density profile produced by charges on confining gates should be relatively smooth, so that the spatial separation between the outer most EC and the second EC should be relatively large at this point, and the Coulomb coupling between the channels, screened by the gates, should be relatively weak. As the electron density is increased, the inner EC should move closer to the outer edge, and the coupling should become stronger, and it is plausible

that by the time the device enters the $\nu = 3$ plateau, the value of K_{12}/K_1 is close to 1.

Further increases in the density should produce additional ECs, which are totally reflected at the QPCs and do not contribute directly to the transport. The number of electrons on any additional closed ECs, as on other localized states, will be restricted to integer values, and in principle, due to Coulomb interactions, there should be a jump in the interference phase of outer edge states each time this integer changes by one. However, Coulomb interactions in our system are strongly screened by the nearby gates, so if the additional channels are not close to the outer two ECs, the jumps would be too small to be observable. In monolayer graphene, the energy gap at $\nu = 2$, which is due to the cyclotron energy, is much larger than the gaps at $\nu = 1, 3, 4$, and 5, which arise from electron-electron interactions. Consequently, we expect that the spatial separation between the outermost EC and the second EC will tend to be small compared to the separation between the second EC and any additional ECs.

Another issue is the stability criterion embodied in the requirement $|K_{12}|^2 \le K_1 K_2$. This requirement is automatically satisfied if we assume that when the two outer ECs are close together, the energy for adding an electron to either one of them is dominated by an electrostatic energy that depends primarily on the total charge on the edges, and only weakly on the difference between them, so that $E = a\delta Q_1{}^2 + b\delta Q_2{}^2 + 2K_{12}(\delta Q_1 + \delta Q_2)^2$, with a and b small compared to K_{12}. Then, K_1 and K_2 will be approximately equal to each other and slightly larger than K_{12}.

This analysis is compatible with experiments in GaAs interferometers where the ECs occur at the boundary between two QHE states of different integer filling fractions (ref. 27). There it was found that the $h/2e$ periodicity occurred only if the outer EC and second EC belong to the same orbital Landau level, and not if they belong to different levels. In the first case, the energy gap for the QHE state between the two ECs will arise from electron-electron interactions, while the energy gap in the second case will be dominated by the generally larger cyclotron energy. Therefore, in the first case, when the density is increased enough to populate a third QHE state in the bulk of the sample, the two outer ECs might be pushed so close to each other that they are strongly coupled, while this might not be expected to happen in the second case.

Physics of AB frequency doubling at strong coupling

The meaning of the charge fluctuations δQ_1 and δQ_2 can be made more precise as follows. As stated in the main text, we define Q_1 as the number of electrons in the lowest spin-split Landau level enclosed by the outer edge mode and Q_2 as the number of electrons in the higher spin state enclosed by the inner mode. These charges are related to the enclosed areas A_1 and A_2 by $Q_i = A_i B/\Phi_0$, where $i = 1$ or 2. These areas are allowed to deviate slightly from the ideal areas $\bar{A}_i$, which are assumed to be smooth functions of V_{PG} and, at most weakly varying functions of B and V_{MG}. Then $\delta Q_i = Q_i - B\bar{A}_i/\Phi_0$, and the energy E may be expanded to quadratic order in δQ_i as stated above.

When the inner mode is completely reflected at the QPC, the charge Q_2 is constrained to be an integer, while the charge Q_1 can change continuously, assuming that the outer edge is mostly transmitted through the QPCs. At low temperatures the charges will be determined so as to minimize E, subject to the integer constraint.

If Q_2 is held fixed while the magnetic field is increased by a small amount dB, the inner edge charge δQ_2 will change by an amount $-dB\bar{A}_2/\Phi_0$. This happens because, as the area shrinks, charge is transferred from the edge region to the interior, where it is effectively screened by the gates, leaving a charge deficit at the edge. In the strong coupling limit, this will cause δQ_1 to increase by an equal amount. Thus, the total charge Q_1 in the lowest spin-split Landau level will increase by $dQ_1 = dB(\bar{A}_1 + \bar{A}_2)/\Phi_0$, and the interferometer phase θ will increase by $2\pi dQ_1$.

If B is increased by a large amount, the value of Q_2 will not be fixed but will undergo periodic integer jumps. In the strong coupling limit, the jump in Q_1 caused by a jump in Q_2 will also be an integer. This will cause θ to jump by a multiple of 2π, which will be invisible in an interferometer experiment. Thus, the observed rate of change of the phase will be $d\theta/dB = 2\pi(\bar{A}_1 + \bar{A}_2)/\Phi_0$, which is equal to $4\pi\bar{A}_1/\Phi_0$, if we neglect the difference between $\bar{A}_1$ and $\bar{A}_2$. This rate of change is twice as fast as would have been observed in the absence of coupling between the inner and outer edge modes.

We remark that in the course of adding one flux quantum to the area $\bar{A}_1$, one would expect on average to have a jump by one electron in each spin state. So, in general, one will have one positive jump in Q_2 and one negative jump in Q_1. Thus, while the observed interference phase will change by an amount equivalent to a change of two electrons, the actual change in Q_1 will only be one electron.

Influence of bulk-edge coupling and screening by nearby gates

Screening of long-range Coulomb interactions by nearby gates in our device is essential to consider when determining the influence of edge-edge and bulk-edge coupling on the interference signal. In the data analysis and preceding discussion, we have neglected bulk-edge coupling since the radius of the interference loop extracted from the outer EC interference (~600 nm) is always much larger than the average distance to the graphite screening gates (~38 nm), as shown in Supplementary Fig. 9. Therefore, bulk-edge interaction should be well screened by the gates. In contrast, the distance between the inner and outer EC approaches ~85 nm in the strong-coupling limit, which enables strong Coulomb interaction that will not be screened out by the gates. We also observe that the contribution of edge-edge coupling, as evidenced by the presence of the $\boldsymbol{f}_{o+i}$ component in the signal, becomes significant only when the edge-edge separation becomes about 200 nm or less, within about a factor of 5 of the gate distance. The behavior of the inner EC interference over the range of density we explored is also consistent with these rough estimates, as the interference signal continues to show Aharonov-Bohm interference (Supplementary Fig. 8) through a shrinking area down to an enclosed radius of 200 nm. Hence, we find that bulk-edge coupling is negligible in all experimental regimes that we explored.

According to the model by Frigeri et al. (ref. 33), for negligible bulk-edge coupling, the transition to frequency doubling occurs when the inter-channel interaction drops to roughly half of the charging energy for a bare outer EC. This would correspond to the point where the inter-channel distance is comparable to the distance to the screening gates. We find that indeed this agrees with our data, since the system enters the strongly coupled limit when the average inter-channel separation approaches ~85 nm, approximately twice the average distance to the top and bottom gates (Supplementary Fig. 9).

Robustness of the theoretical predictions

As discussed in ref. 36, when a single EC passes through the two constrictions, with weak backscattering at the constrictions, the interference phase seen at low temperatures and low source-drain voltage is given by $\theta = 2\pi Q + \theta_0$, mod 2π, where Q is the total electron charge (in units e) in the region between the two scattering points (the expectation value of the charge on the interferometer in its ground state) and θ_0 is a constant for small variations in B, V_{PG}, and V_{MG}. The argument is essentially the same if the backscattering is not weak. The principal effect of stronger backscattering at the QPCs is to add a term to the energy E that favors integer values of the charge Q_1 and hence integer values of the total charge on the interferometer. This means that as the control parameters are varied continuously, the phase difference $\theta - \theta_0$ will undergo an additional modulation pulling it towards the nearest integer multiple of 2π. If we define θ_b as the value of the interferometer phase that would occur in the limit of weak backscattering, for the given value of the control parameters, then the

actual value of θ should have the form $\theta = \theta_b + \delta\theta$, where $\delta\theta$ is a periodic function of $\theta_b - \theta_0$. In addition, in the presence of finite back scattering, interference contribution to the measured resistivity may no longer be a simple sinusoidal function of θ but can contain higher harmonics. The combination of these effects means that the interference current will remain a periodic function of θ_b, with period 2π, but the relative amplitudes of various harmonics may be modified. In the main text, it was argued that $\cos\theta_b$ should be a two-dimensional periodic function of B and the gate voltages, with frequencies expressed in terms of two non-colinear fundamental vectors in reciprocal parameter space. The effect of finite backscattering at the QPCs will be to modify the amplitudes of the various Fourier components, but not to change their positions.

Using similar arguments, we may argue that measurement at finite temperature should not change the locations of the fundamental frequency vectors, but thermal fluctuations will reduce the Fourier amplitudes. In general, at high temperatures T, the amplitude of a given Fourier component will fall off, proportional to $e^{-T/\varepsilon}$, where ε will be different for each Fourier component. At sufficiently high temperatures, therefore, only the one or two components with the largest values of ε will remain visible. The values of ε will depend on details of the system, but typically the Fourier components that are most prominent at $T = 0$ will be the ones that persist to highest temperatures.

For our system, in the case where there is only a single EC, as we find for bulk filling less than 2, the value of ε for the lowest Fourier mode is predicted to be $\varepsilon = h\upsilon/(2\pi^2 P)$, where υ is the EC velocity and P is the perimeter of the interferometer path. For the case of two strongly coupled edge channels, the prediction is $\varepsilon = h\upsilon/(4\pi^2 P)$, where υ is now the velocity of the fast charge mode. In both cases, the dominant effects come from thermal fluctuations $e\delta Q$ of the charge on the edge, whose energy cost is given by $(e\delta Q)^2/(2\gamma P)$, where γ is the capacitance per unit length of the edge. The velocity υ is given by $\upsilon = \delta\sigma_{xy}/\gamma$, where $\delta\sigma_{xy}$ is the change in Hall conductance across the edge. Using our lithographically defined perimeter $P = 4.24\mu m$ and the velocity $\upsilon_e = \frac{e\Delta V_b P}{h} = 1.46\times10^5 m/s$ extracted from finite-bias dependence in the uncoupled case (Supplementary Fig. 11), we find $\varepsilon = 83.7mK$, well above our estimated electron temperature.

Data availability

The transport data presented in this manuscript are available at the online repository Zenodo, available at https://doi.org/10.5281/zenodo.11640994.

Code availability

The code used to analyze the data presented in this manuscript is available at the online repository Zenodo, available at https://doi.org/10.5281/zenodo.11640994.

References

1. Giamarchi, T. *Quantum Physics in One Dimension*. (Clarendon Press, 2003).
2. Wen, X.-G. *Quantum Field Theory of Many-Body Systems: From the Origin of Sound to an Origin of Light and Electrons*. (Oxford University Press, Oxford, New York, 2007).
3. Marguerite, A. et al. Imaging work and dissipation in the quantum Hall state in graphene. *Nature* **575**, 628–633 (2019).
4. Uri, A. et al. Nanoscale imaging of equilibrium quantum Hall edge currents and of the magnetic monopole response in graphene. *Nat. Phys.* **16**, 164–170 (2020).
5. Halperin, B. I. Quantized Hall conductance, current-carrying edge states, and the existence of extended states in a two-dimensional disordered potential. *Phys. Rev. B* **25**, 2185–2190 (1982).
6. Chklovskii, D. B., Shklovskii, B. I. & Glazman, L. I. Electrostatics of edge channels. *Phys. Rev. B* **46**, 4026–4034 (1992).
7. Kim, S. et al. Edge channels of broken-symmetry quantum Hall states in graphene visualized by atomic force microscopy. *Nat. Commun.* **12**, 2852 (2021).
8. Coissard, A. et al. Absence of edge reconstruction for quantum Hall edge channels in graphene devices. *Sci. Adv.* **9**, eadf7220 (2023).
9. Ji, Y. et al. An electronic Mach–Zehnder interferometer. *Nature* **422**, 415–418 (2003).
10. Bocquillon, E. et al. Electron quantum optics in ballistic chiral conductors. *Ann. der Phys.* **526**, 1–30 (2014).
11. van Wees, B. J. et al. Observation of zero-dimensional states in a one-dimensional electron interferometer. *Phys. Rev. Lett.* **62**, 2523–2526 (1989).
12. de C. Chamon, C., Freed, D. E., Kivelson, S. A., Sondhi, S. L. & Wen, X. G. Two point-contact interferometer for quantum Hall systems. *Phys. Rev. B* **55**, 2331–2343 (1997).
13. Halperin, B. I., Stern, A., Neder, I. & Rosenow, B. Theory of the Fabry-P\'erot quantum Hall interferometer. *Phys. Rev. B* **83**, 155440 (2011).
14. Nakamura, J., Liang, S., Gardner, G. C. & Manfra, M. J. Direct observation of anyonic braiding statistics. *Nat. Phys.* **16**, 931–936 (2020).
15. Nakamura, J., Liang, S., Gardner, G. C. & Manfra, M. J. Impact of bulk-edge coupling on observation of anyonic braiding statistics in quantum Hall interferometers. *Nat. Commun.* **13**, 344 (2022).
16. Carrega, M., Chirolli, L., Heun, S. & Sorba, L. Anyons in quantum Hall interferometry. *Nat. Rev. Phys.* **3**, 698–711 (2021).
17. Feldman, D. E. & Halperin, B. I. Fractional charge and fractional statistics in the quantum Hall effects. *Rep. Prog. Phys.* **84**, 076501 (2021).
18. Ronen, Y. et al. Aharonov–Bohm effect in graphene-based Fabry–Pérot quantum Hall interferometers. *Nat. Nanotechnol.* **16**, 563–569 (2021).
19. Déprez, C. et al. A tunable Fabry–Pérot quantum Hall interferometer in graphene. *Nat. Nanotechnol.* **16**, 555–562 (2021).
20. Fu, H. et al. Aharonov–Bohm Oscillations in Bilayer Graphene Quantum Hall Edge State Fabry–Pérot Interferometers. *Nano Lett.* **23**, 718–725 (2023).
21. Zhao, L. et al. Graphene-based quantum hall interferometer with self-aligned side gates. *Nano Lett.* **22**, 9645–9651 (2022).
22. Zhang, Y. et al. Distinct signatures for Coulomb blockade and Aharonov-Bohm interference in electronic Fabry-Perot interferometers. *Phys. Rev. B* **79**, 241304 (2009).
23. Ofek, N. et al. Role of interactions in an electronic Fabry–Perot interferometer operating in the quantum Hall effect regime. *Proc. Natl Acad. Sci.* **107**, 5276–5281 (2010).
24. Sivan, I. et al. Observation of interaction-induced modulations of a quantum Hall liquid's area. *Nat. Commun.* **7**, 12184 (2016).
25. Choi, H. K. et al. Robust electron pairing in the integer quantum hall effect regime. *Nat. Commun.* **6**, 7435 (2015).
26. Sivan, I. et al. Interaction-induced interference in the integer quantum Hall effect. *Phys. Rev. B* **97**, 125405 (2018).
27. Biswas, S., Kundu, H. K., Umansky, V. & Heiblum, M. Electron pairing of interfering interface-based edge modes. *Phys. Rev. Lett.* **131**, 096302 (2023).
28. Demir, A. et al. Correlated double-electron additions at the edge of a two-dimensional electronic system. *Phys. Rev. Lett.* **126**, 256802 (2021).
29. Keimer, B., Kivelson, S. A., Norman, M. R., Uchida, S. & Zaanen, J. From quantum matter to high-temperature superconductivity in copper oxides. *Nature* **518**, 179–186 (2015).
30. Willett, R. L. The quantum Hall effect at 5/2 filling factor. *Rep. Prog. Phys.* **76**, 076501 (2013).
31. Li, J. I. A. et al. Even-denominator fractional quantum Hall states in bilayer graphene. *Science* **358**, 648–652 (2017).
32. Huang, K. et al. Valley isospin controlled fractional quantum hall states in bilayer graphene. *Phys. Rev. X* **12**, 031019 (2022).

33. Frigeri, G. A., Scherer, D. D. & Rosenow, B. Sub-periods and apparent pairing in integer quantum Hall interferometers. *EPL* **126**, 67007 (2019).
34. Büttiker, M. Quantized transmission of a saddle-point constriction. *Phys. Rev. B* **41**, 7906–7909 (1990).
35. Zimmermann, K. et al. Tunable transmission of quantum Hall edge channels with full degeneracy lifting in split-gated graphene devices. *Nat. Commun.* **8**, 14983 (2017).
36. Feldman, D. E. & Halperin, B. I. Robustness of quantum Hall interferometry. *Phys. Rev. B* **105**, 165310 (2022).
37. Röösli, M. P. et al. Observation of quantum Hall interferometer phase jumps due to a change in the number of bulk quasiparticles. *Phys. Rev. B* **101**, 125302 (2020).
38. Yang, W. et al. Evidence for correlated electron pairs and triplets in quantum Hall interferometers. Preprint at http://arxiv.org/abs/2312.14767 (2023).
39. Shavit, G. & Oreg, Y. Electron pairing induced by repulsive interactions in tunable one-dimensional platforms. *Phys. Rev. Res.* **2**, 043283 (2020).
40. Frigeri, G. A. & Rosenow, B. Electron pairing in the quantum Hall regime due to neutralon exchange. *Phys. Rev. Res.* **2**, 043396 2020).
41. Inoue, H. et al. Charge Fractionalization in the Integer Quantum Hall Effect. *Phys. Rev. Lett.* **112**, 166801 (2014).
42. Wei, Z., Feldman, D. E. & Halperin, B. I. Quantum Hall interferometry at finite bias with multiple edge channels. Preprint at https://arxiv.org/abs/2405.05486v1 (2024).
43. Altimiras, C. et al. Non-equilibrium edge-channel spectroscopy in the integer quantum Hall regime. *Nat. Phys.* **6**, 34–39 (2010).
44. Bocquillon, E. et al. Separation of neutral and charge modes in one-dimensional chiral edge channels. *Nat. Commun.* **4**, 1839 (2013).
45. Freulon, V. et al. Hong-Ou-Mandel experiment for temporal investigation of single-electron fractionalization. *Nat. Commun.* **6**, 6854 (2015).
46. Hashisaka, M., Hiyama, N., Akiho, T., Muraki, K. & Fujisawa, T. Waveform measurement of charge- and spin-density wavepackets in a chiral Tomonaga–Luttinger liquid. *Nat. Phys.* **13**, 559–562 (2017).
47. Willett, R. L. et al. Interference measurements of Non-Abelian e/4 & Abelian e/2 Quasiparticle Braiding. *Phys. Rev. X* **13**, 011028 (2023).
48. Kundu, H. K., Biswas, S., Ofek, N., Umansky, V. & Heiblum, M. Anyonic interference and braiding phase in a Mach-Zehnder interferometer. *Nat. Phys.* **19**, 515–521 (2023).
49. Nakamura, J., Liang, S., Gardner, G. C. & Manfra, M. J. Fabry-P\'erot Interferometry at the v =2/5 fractional quantum hall state. *Phys. Rev. X* **13**, 041012 (2023).
50. Nakamura, J., Liang, S., Gardner, G. C. & Manfra, M. J. Fabry-Pérot Interferometry at the v = 2 / 5 fractional quantum hall state. *Phys. Rev. X* **13**, 041012 (2023).
51. Kim, J. et al. Aharonov-Bohm interference and the evolution of phase jumps in fractional quantum Hall Fabry-Perot interferometers based on bi-layer graphene. Preprint at https://arxiv.org/abs/2402.12432v1 (2024).
52. Werkmeister, T. et al. Anyon braiding and telegraph noise in a graphene interferometer. Preprint at https://arxiv.org/abs/2403.18983v2 (2024).
53. Samuelson, N. L. et al. Anyonic statistics and slow quasiparticle dynamics in a graphene fractional quantum Hall interferometer. Preprint at https://arxiv.org/abs/2403.19628v1 (2024).

Acknowledgements

We thank Andrew Pierce and Raymond Ashoori for helpful comments in the early stages of this work. We also thank Raymond Ashoori for lending important cryostat parts used in this measurement and Jim MacArthur for building electronics used in our experiment. P.K., T.W., and Y.R. acknowledge support from DOE (DE-SC0012260) for sample preparation, measurement, characterization, and analysis. J.R.E. acknowledges support from ARO MURI (N00014-21-1-2537) for sample preparation, measurement, characterization, and analysis. K.W. and T.T. acknowledge support from the Elemental Strategy Initiative conducted by the MEXT, Japan, Grant Number JPMXP0112101001, JSPS KAKENHI Grant Number JP20H00354 and the CREST(JPMJCR15F3), JST. D.E.F. and Z.W. acknowledge support by the National Science Foundation under Grant No. DMR-2204635. B.I.H. acknowledges support from NSF grant DMR-1231319. M.E.W. and A.Y. acknowledge support from Quantum Science Center (QSC), a National Quantum Information Science Research Center of the U.S. Department of Energy. Nanofabrication was performed at the Center for Nanoscale Systems at Harvard, supported in part by an NSF NNIN award ECS-00335765.

Author contributions

T.W. and D.N. stacked the graphite-encapsulated heterostructures. T.W. performed the nanofabrication, measurements, and data analysis. J.R.E. and Y.R. assisted in the measurement and analysis. D.E.F., B.I.H., and Z.W. contributed the theoretical analysis. M.E.W. and A.Y. provided the measurement cryostat and collaborated on the discussions and analysis. K.W. and T.T. provided the hBN crystals. T.W., B.I.H., J.R.E., and P.K. wrote the paper with input from all authors.

Competing interests

The authors declare no competing interests.

Additional information

Supplementary information The online version contains supplementary material available at https://doi.org/10.1038/s41467-024-50695-1.

Correspondence and requests for materials should be addressed to Philip Kim.

Peer review information *Nature Communications* thanks the anonymous reviewers for their contribution to the peer review of this work. A peer review file is available.